CHAPTER III

Doped strontium hexaferrite-LLDPE composites for design of single layer absorber

Content:

3.1 Introduction

M-type ferrites and its doped versions have high saturation magnetization and crystalline anisotropy, which, when used as fillers in polymer composites form absorbers with high reflection loss [1-7]. Doping of M-type hexaferrites with other metals improves its material properties viz. ε_r and μ_r [6-8] as required for good absorption. The magnetic properties of strontium hexaferrite can be modified by substituting stoichiometrically either Sr^{2+} ion or Fe^{3+} ions with other metal ions [1, 4, 5, 8-10]. The intrinsic magnetic properties of hexaferrite can be significantly improved by substituting Fe^{3+} in different sites of hexaferrite with other suitable ions, such as Co^{2+}, Cr^{3+}, Ti^{4+}, Al^{3+} [7, 11-13].

Aluminium substituted M-type hexagonal ferrite is reported to have large field anisotropy [14] while cobalt is a fast relaxer owing to its degenerate energy states which enhances the microwave properties [15, 16]. Nanosized strontium ferrite doped with cobalt and aluminium are synthesized and used as magnetic filler in LLDPE matrix. For $SrAl_xFe_{12-x}O_{19}$, x is initially increased from 0.2 to 0.8 in steps of 0.2. However, no appreciable change in microwave absorption properties are observed and hence the results are not included here. But, when x is increased from 1 to 3, changes in microwave absorption properties are observed. Therefore, the composites for these variations are studied. For $SrCo_xFe_{12-x}O_{19}$, x is increased from 0.2 to 1.2 in steps of 0.2. Microstructural, magnetic, thermal and microwave characterizations is carried out using methods mentioned in section 2.2 and 2.3, chapter II. Water absorbance and density are also investigated. The developed composites are then designed as single layer absorber using the transmission line model in X-band and fabricated.

3.2 Synthesis and characterizations

Nanosized doped strontium ferrite is synthesized using co-precipitation technique, followed by the microstructural studies of the synthesized nanoparticles and nanocomposites. XRD, TEM and FTIR analysis is carried. Composites with 60 wt. % of filler in LLDPE matrix are fabricated and homogeneity of distributions is ascertained from SEM images.

3.2.1 Material synthesis and composite preparation

Nano-sized $SrAl_xFe_{12-x}O_{19}$ (x = 1.0, 2.0, 3.0) are prepared stoichiometrically according to the composition using aluminium nitrate (≥ 98%) and cobalt nitrate hexahydrate (≥ 98%) for $SrCo_xFe_{12-x}O_{19}$ (x = 0.2, 0.4, 0.6, 0.8, 1.0, 1.2) along with strontium nitrate (≥ 98%) and iron (III) nitrate nonahydrate (≥ 98%) dissolved in de-ionized water. The solution is stirred continuously for an hour at 80˚C followed by dropwise addition of NaOH to control the size of the particles. Thereafter, oleic acid is added to prevent agglomeration. A brownish precipitate is formed, which is repeatedly washed with a distilled water-ethanol solution to remove traces of sodium and nitrate compounds. The mixed oxides of the starting materials are removed by annealing the dried powder at a temperature of 1000˚C in a furnace for 3 hours. Thereafter, size and shape of $SrAl_xFe_{12-x}O_{19}$ and $SrCo_xFe_{12-x}O_{19}$ particles are determined using XRD and TEM studies.

Composite specimens of 60 wt. % are fabricated by mixing LLDPE powder with developed ferrite samples in situ. Composite pellets are made by die-moulding using hot-press technique as described in section 2.2.1, chapter II.

3.2.2 Microstructural characterizations

X-ray diffraction (XRD)

XRD pattern of the synthesized $SrAl_xFe_{12-x}O_{19}$ and $SrCo_xFe_{12-x}O_{19}$ powder is obtained at room temperature over a 2θ angle from 20˚ to 70˚ which is shown in figure 3.1.

Diffraction planes, (0 0 6), (1 0 6), (1 1 0), (0 0 8), (1 0 7), (1 1 4), (1 0 8), (2 0 3), (1 0 10), (3 0 0), (2 1 7), (2 2 0) and (2 0 14) corresponds to diffraction peaks at 2θ values of 20.1˚, 26.30˚, 30.34˚, 32.47˚, 33.27˚, 34.47˚, 35.20˚, 40.45˚, 48.68˚, 52.2˚, 55.38˚, 61.19˚, 67.65˚ indicates M-type hexagonal structure of the $SrAl_xFe_{12-x}O_{19}$ as seen from the figure 3.1. The planes are determined from JCPDS card number 33-1340. No characteristic plane of aluminium ions is observed confirming that the aluminium ions enter the lattice of strontium ferrite as the ionic radius of aluminium ion (0.0535 nm) is less than that of iron ions (0.065 nm) [14]. Aluminium replaces the iron mostly in the octahedral sites (12k, $4f_2$, 2a) [17].

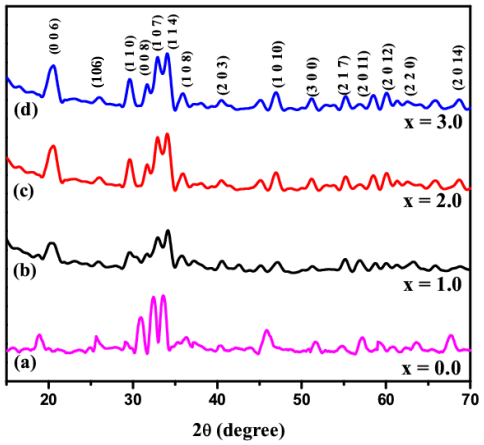

Figure 3.1: XRD pattern of $SrAl_xFe_{12-x}O_{19}$

Figure 3.2, shows diffraction peaks at 2θ values of 21.06˚, 26.30˚, 29.8˚, 30.34˚, 32.47˚, 34.27˚, 35.47˚, 36.3˚, 39.19˚, 42.45˚, 48.68˚, 52.21˚, 55.38˚, 57.88˚, 60.12˚, 63.19˚, 67.65˚ and corresponds to the strongest diffraction planes (0 0 6), (1 0 6), (1 1 0), (0 0 8), (1 0 7), (1 1 4), (2 0 0), (2 0 3), (2 0 5), (2 0 6), (1 0 11), (2 0 9), (2 1 7), (2 0 11), (2 0 12), (2 2 0) and (2 0 1 4). These peaks correspond to hexagonal Sr-M type hexaferrite phase (JCPDS # 39-1346). No other phase is observed indicating that the structure is stable.

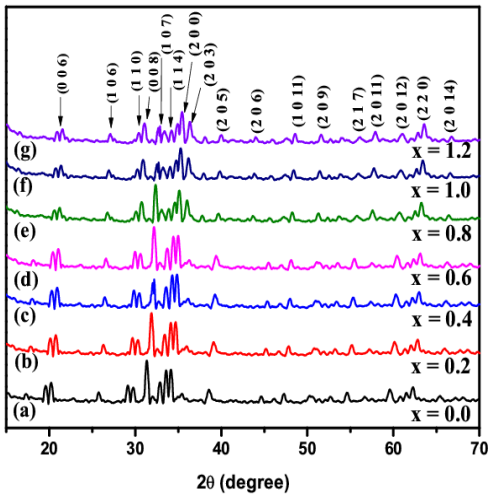

Figure 3.2: XRD pattern of $SrCo_xFe_{12-x}O_{19}$

Cobalt ions preferably occupy the octahedral $4f_2$ and 2a sites for the Fe ions. Such behavior has also been observed in references [11, 18]. The d-spacing of the strontium ferrite is calculated using Bragg's equation. Peaks for cobalt ions are not found in the spectra indicating that cobalt ions enters into the crystal sites of the hexaferrite structure. The calculated lattice parameters are close to M-type hexaferrite phase (a = 5.88 Å and c = 23.05 Å). The average crystalline size is in

nanometer range (Table 3.1 (a)). Gradual shift of the peaks towards right indicates substitution of aluminium and cobalt ions entering the lattice structure of hexaferrite.

Table 3.1: Crystalline size (D) and lattice parameter of $SrAl_xFe_{12-x}O_{19}$ and $SrCo_xFe_{12-x}O_{19}$

Ferrite compositions	Average crystalline size (nm)	Lattice parameters (Å)		D (008) (nm)	D (107) (nm)	D (107)/ D (008) (nm)
		a	c			
$SrAlFe_{11}O_{19}$	20.13	5.86	23.03	24.74	15.75	0.64
$SrAl_2Fe_{10}O_{19}$	20.54	5.88	23.04	20.56	17.42	0.85
$SrAl_3Fe_9O_{19}$	21.28	5.88	23.05	20.36	18.13	0.89
$SrCo_{0.2}Fe_{11.8}O_{19}$	24.39	5.83	23.01	24.98	23.23	0.93
$SrCo_{0.4}Fe_{11.6}O_{19}$	25.12	5.83	23.02	25.85	24.56	0.95
$SrCo_{0.6}Fe_{11.4}O_{19}$	27.78	5.87	23.03	27.81	26.69	0.96
$SrCo_{0.8}Fe_{11.2}O_{19}$	30.01	5.88	23.07	29.63	28.76	0.97
$SrCo_{1.0}Fe_{11}O_{19}$	32.96	5.88	23.08	30.11	29.50	0.98
$SrCo_{1.2}Fe_{10.8}O_{19}$	33.07	5.87	23.08	32.83	32.52	0.99

From Table 3, it is seen that with increase in the doping ions, there is an increase in the crystallite size for aluminium doped strontium ferrite. It is reported that the crystallite growth orientation of $SrFe_{12-x}Al_xO_{19}$ is determined by taking the ratios of the reflection planes parallel (1 0 7) and perpendicular (0 0 8) to c-axis [19]. From Table 3.1 (b), it is observed that the ratio D (1 0 7)/D (0 0 8) increases from 0.63 to 0.89 with aluminium ion doping from x=1 to 3. This value suggests that the $SrFe_{12-x}Al_xO_{19}$ crystals tends to grow preferentially along [1 0 1] direction with increase in the doping level. An increase in size along c-axis is observed with aluminium content leading to increase in the grain size.

Fourier-transform infrared spectroscopy (FTIR)

The FTIR spectroscopy study of $SrAl_xFe_{12-x}O_{19}$ and $SrCo_xFe_{12-x}O_{19}$ powders conducted to ascertain the bond structure of the synthesized ferrites and interactions among the various constituents in the composites are given in figure 3.3 and figure 3.4. Al–O bending vibrations is observed in the wave number bands in the range 550-603 cm^{-1} and 447-457 cm^{-1} show the presence of Fe–O stretching vibrations which corresponds to the formation of tetrahedral and octahedral clusters. Also, the bands existing in the 891-900 cm^{-1} range represent Sr–O stretching. Broad absorption peaks at 1500 cm^{-1} and 3450 cm^{-1}, corresponds to characteristic O–H stretching band which this is due to water molecules adsorbed to the very finely

dispersed samples [20]. The peaks at ~1630 cm^{-1} and 3434 cm^{-1} exhibits the stretching vibration of hydrogen bonded -OH group. The peaks at about 900 cm^{-1} and 1415 cm^{-1} corresponds to the Co-O stretching vibration. These two peaks become increasingly stronger as *x* increases. Interestingly with increasing amount of added cobalt, the peaks at about 450 cm^{-1} and 600 cm^{-1} are stronger [18] as the chemical polarization of the internal chemical bonds for $SrFe_{12}O_{19}$ is greatly strengthened by doping cobalt into the $SrFe_{12}O_{19}$ as Fe-O-Co and Sr-O-Co chemical bonds could be formed. Consequently, the oxygen atom of Fe (Sr)-O bond might be shared with cobalt atom, which probably contributes to vibrational coupling between Fe (Sr)-O and Co-O leading to stronger and sharper peaks.

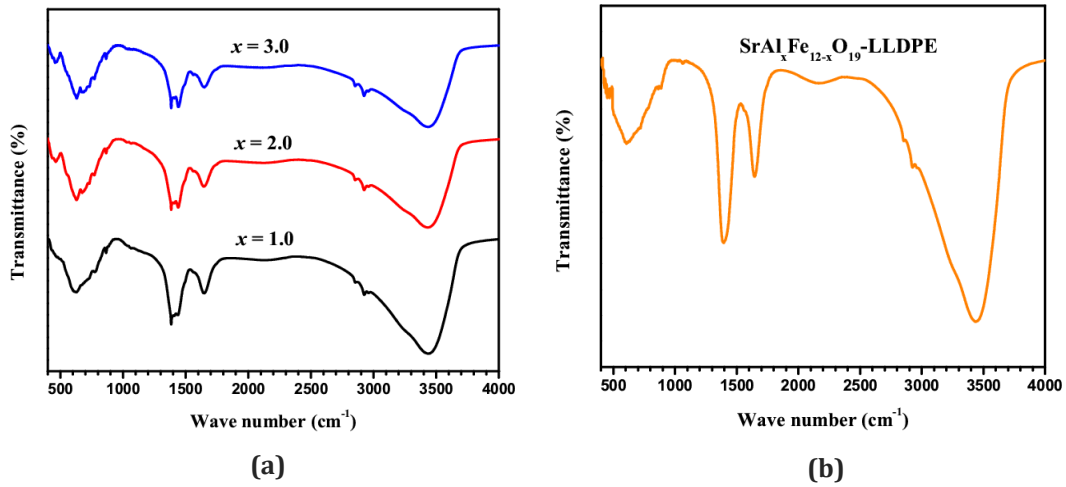

Figure 3.3: FTIR spectra **(a)** $SrAl_xFe_{12-x}O_{19}$ (x=1.0- 3.0) **(b)** $SrAl_xFe_{12-x}O_{19}$-LLDPE composite

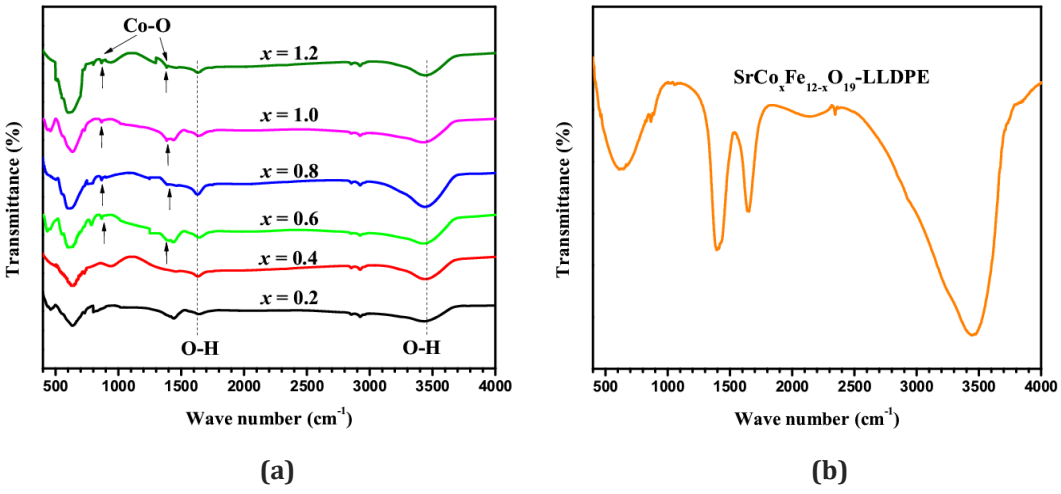

Figure 3.4: FTIR spectra **(a)** $SrCo_xFe_{12-x}O_{19}$ (x=0.2- 1.2) **(b)** $SrCo_xFe_{12-x}O_{19}$-LLDPE composite

This also indicates that cobalt ion is combined with the internal structure of $SrFe_{12}O_{19}$. In the FTIR spectrum of the composite, the peak at about 900 cm^{-1}

corresponds to the Co-O stretching. At about 1463 cm^{-1}, CH_2 bond stretching is observed. The spectrum of both the composites show the presence of both phases of fillers and the matrix and no new peaks has been observed.

Transmission electron microscopy (TEM)

The TEM images of $SrAl_xFe_{12-x}O_{19}$ and $SrCo_xFe_{12-x}O_{19}$ for different values of *x* in figures 3.5 (a-c) and 3.6 (a-f) show extended rod like structure. Particle lengths of ~77 and ~78 nm is observed for the two doped versions of strontium ferrite.

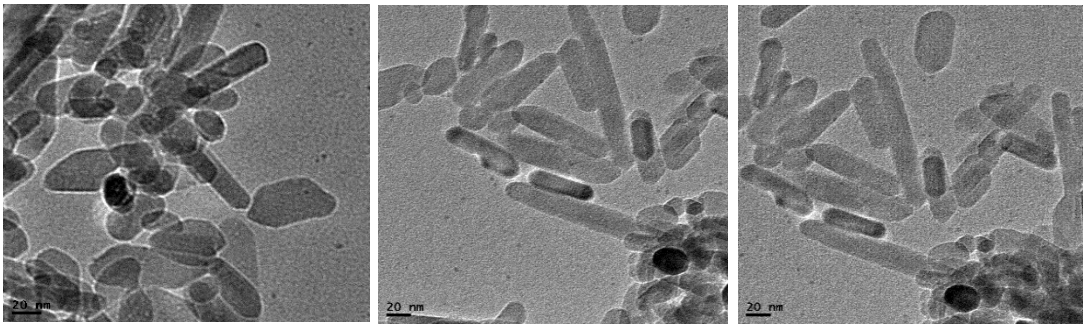

(a) **(b)** **(c)**

Figure 3.5: $SrAl_xFe_{12-x}O_{19}$ TEM images **(a)** *x*=1.0, **(b)** *x*=2.0, **(c)** *x*=3.0

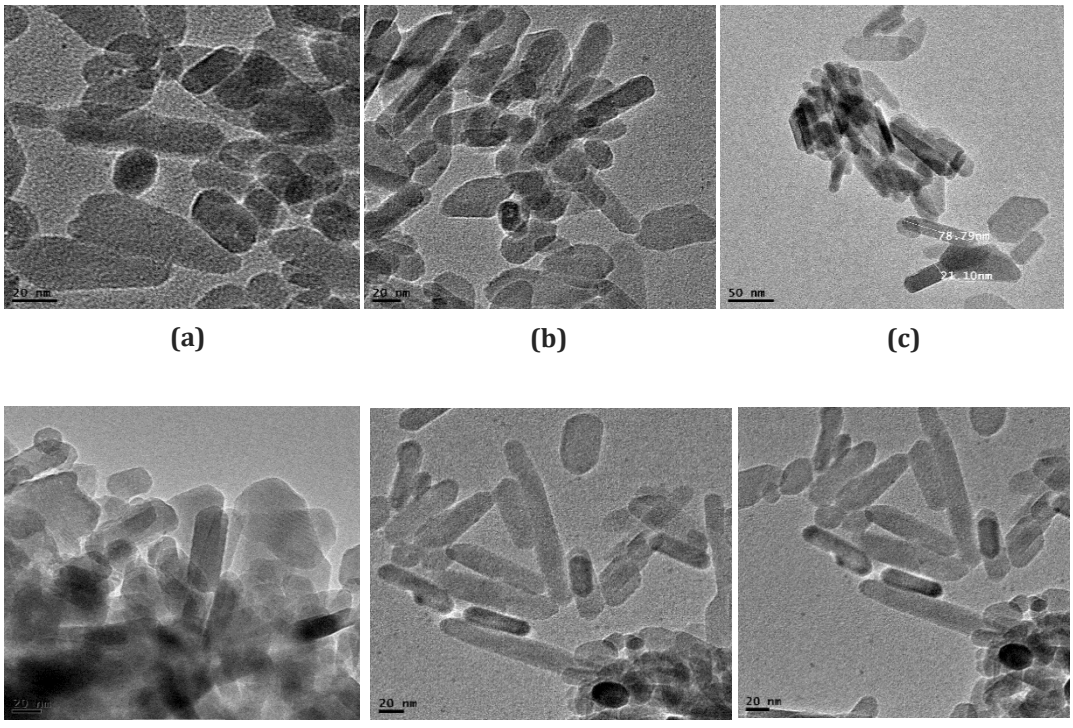

(a) **(b)** **(c)**

(d) **(e)** **(f)**

Figure 3.6: $SrCo_xFe_{12-x}O_{19}$ TEM images **(a)** *x*=0.2, **(b)** *x*=0.4, **(c)** *x*=0.6, **(d)** *x*=0.8, **(e)** *x*=1.0, **(f)** *x*=1.2

Scanning electron microscope (SEM)

SEM images of $SrAl_xFe_{12-x}O_{19}$-LLDPE for x = 1.0, 2.0, 3.0 & $SrCo_xFe_{12-x}O_{19}$-LLDPE for x = 0.2, 0.4, 0.6, 0.8, 1.0, 1.2 given in figure 3.7 (a-c) and 3.8 (a-f) show homogeneity of the composite.

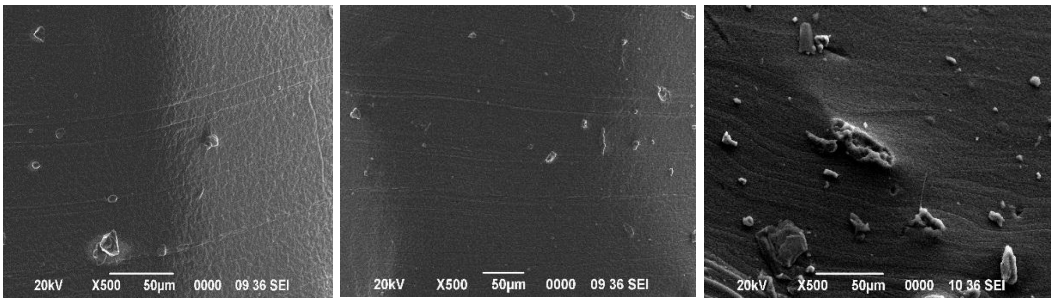

(a) **(b)** **(c)**

Figure 3.7: $SrAl_xFe_{12-x}O_{19}$ SEM images **(a)** x=1.0, **(b)** x=2.0, **(c)** x=3.0

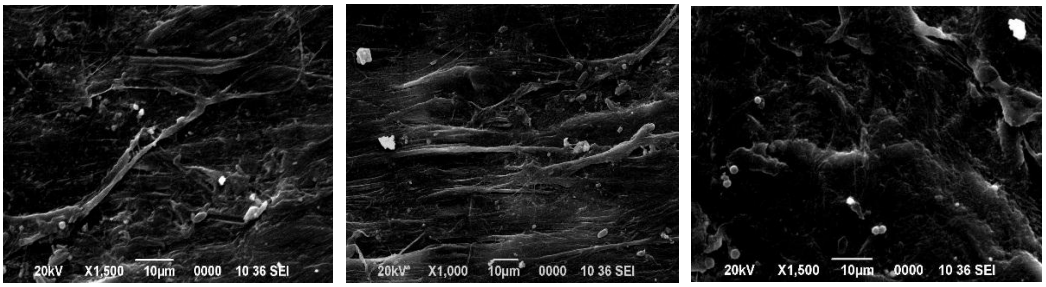

(a) **(b)** **(c)**

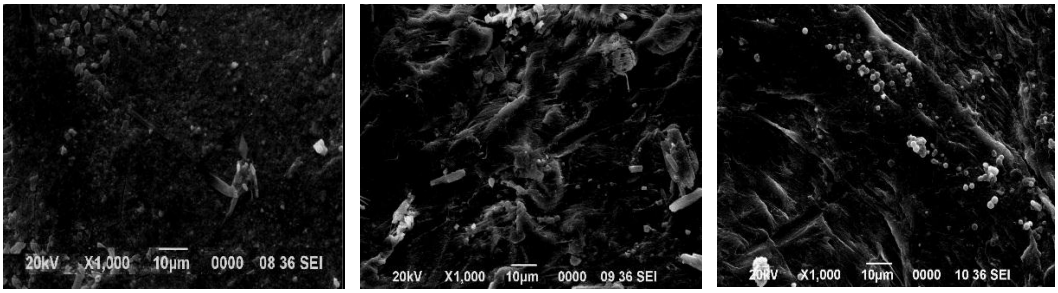

(d) **(e)** **(f)**

Figure 3.8: $SrCo_xFe_{12-x}O_{19}$ SEM images **(a)** x=0.2, **(b)** x=0.4, **(c)** x=0.6, **(d)** x=0.8, **(e)** x=1.0, **(f)** x=1.2

3.2.3 Physical, thermal and magnetic characterizations

Density and Water absorbance

Water absorbance and density of $SrAl_xFe_{12-x}O_{19}$-LLDPE nano-composites and $SrCo_xFe_{12-x}O_{19}$-LLDPE nano-composites for different x values are given in

table 3.2. The water absorption by the composite is insignificant. There is marginal increase in density of the nano-composites with increase in doping in the ferrite content.

Thermo Gravimetric Analysis (TGA)

TGA of the prepared samples of $SrAl_xFe_{12-x}O_{19}$-LLDPE (x = 1.0-3.0) and $SrCo_xFe_{12-x}O_{19}$-LLDPE for (x = 0.2-1.2) is measured in the air atmosphere from room temperature (25˚C) up to 600˚C to determine the decomposition temperatures is shown in figure 3.9.

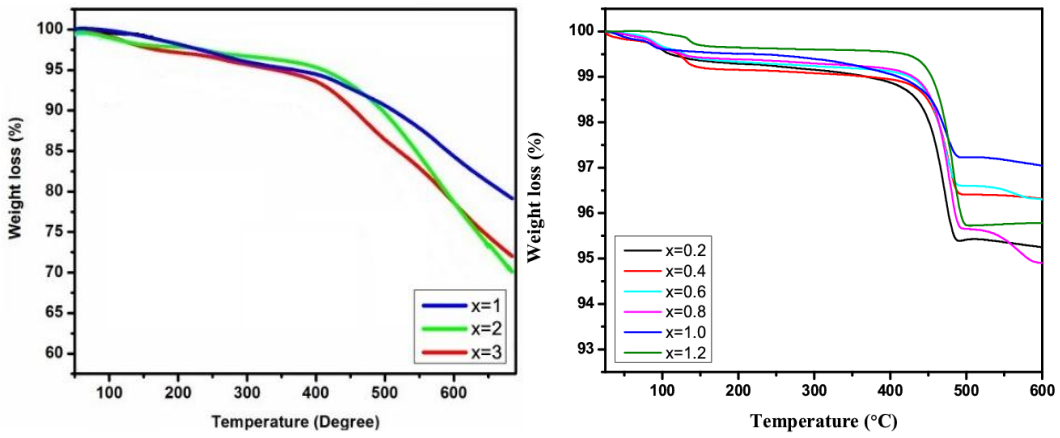

(a) **(b)**

Figure 3.9: TGA curves of the composites for different values of x **(a)** $SrAl_xFe_{12-x}O_{19}$-LLDPE **(b)** $SrCo_xFe_{12-x}O_{19}$-LLDPE

The decomposition temperature of all the composites are found to be around 400˚C with weight loss of 5%. From 400˚C up to 600˚C weight loss is observed, this is due to surface complexes formed during oxidation. Thus, the developed composite are stable almost upto 400˚C before they undergo thermal degradation.

Saturation Magnetization

Hysteresis loops (M-H) at room temperature is measured for $SrCo_{0.8}Fe_{11.2}O_{19}$ powder as shown in figure 3.10.

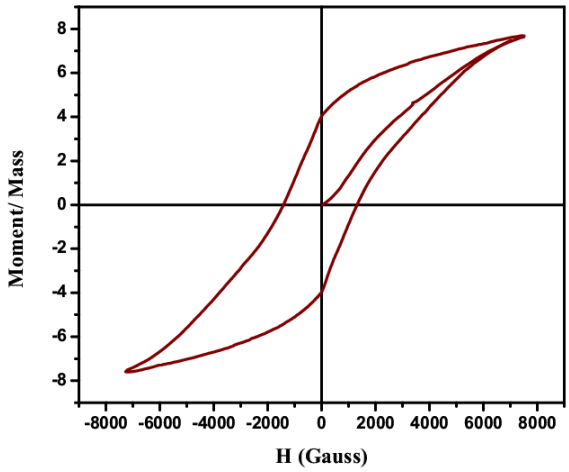

Figure 3.10: Hysteresis loop of $SrCo_{0.8}Fe_{11.2}O_{19}$

The saturation magnetization values of the composites $SrAl_xFe_{12-x}O_{19}$-LLDPE and $SrCo_xFe_{12-x}O_{19}$-LLDPE are given in table 3.2. It is seen that saturation magnetization decreases with increase in aluminium and cobalt content in the strontium ferrite in LLDPE composite.

Table 3.2: Water absorbance, density and $4\pi M_s$ of $SrAl_xFe_{12-x}O_{19}$-LLDPE & $SrCo_xFe_{12-x}O_{19}$ -LLDPE nano-composites

Composition	Water absorbance (%)	Density (g/cc)	$4\pi M_s$ (G)*
$SrAl_xFe_{12-x}O_{19}$-LLDPE			
x=1.0	0.01	1.11	85
x=2.0	0.01	1.28	83
x=3.0	0.02	1.36	82
$SrCo_xFe_{12-x}O_{19}$-LLDPE			
x=0.2	0.02	1.11	102
x=0.4	0.01	1.23	100
x=0.6	0.02	1.29	95
x=0.8	0.01	1.34	87
x=1.0	0.01	1.37	83
x=1.2	0.01	1.38	80

***** *values rounded off to nearest whole number*

3.2.4 Microwave characterization of the developed composite

The real part of the complex permittivity, ε_r' and $tan\ \delta_\varepsilon \left(=\frac{\varepsilon_r''}{\varepsilon_r'}\right)$ of $SrAl_xFe_{12-x}O_{19}$-LLDPE nano-composite for x = 1.0, 2.0, 3.0 (figure 3.11 a and b) and $SrCo_xFe_{12-x}O_{19}$-LLDPE nano-composite for x = 0.2, 0.4, 0.6, 0.8, 1.0, 1.2 (figure 3.12 a, b) are carried out in the frequency range of 8.2-12.4 GHz.

With increase in aluminium ion substitution, ε_r' increases. The maximum ε_r' is observed for the $SrAl_xFe_{12-x}O_{19}$-LLDPE composite with x = 2.0. $SrAl_xFe_{12-x}O_{19}$ in composites have electrons having different locational natural frequencies and damping, leading to different interacting frequencies with the electromagnetic wave, resulting in some variations in ε_r' values. In M-type ferrite, for x ≥1.9, aluminium replaces the iron mostly in the octahedral sites (12k, $4f_2$, 2a) [14]. With increase in the aluminium ions, the exchange phenomenon between Fe^{3+} to Fe^{2+} reduces, thus leading to decrease in complex permittivity values. The resonant behaviour in the relative complex permeability is observed due to natural resonance phenomenon that takes place in the hexaferrite in the GHz range. As reported by Qiu et al. [17], for substitution of aluminium < 1.9, the contributions to the anisotropy constant of iron ions on $4f_2$, 2a and $4f_1$ are relatively small as the iron ions on a 12k site have a negative effect on anisotropy constant, thus reducing the overall field anisotropy.

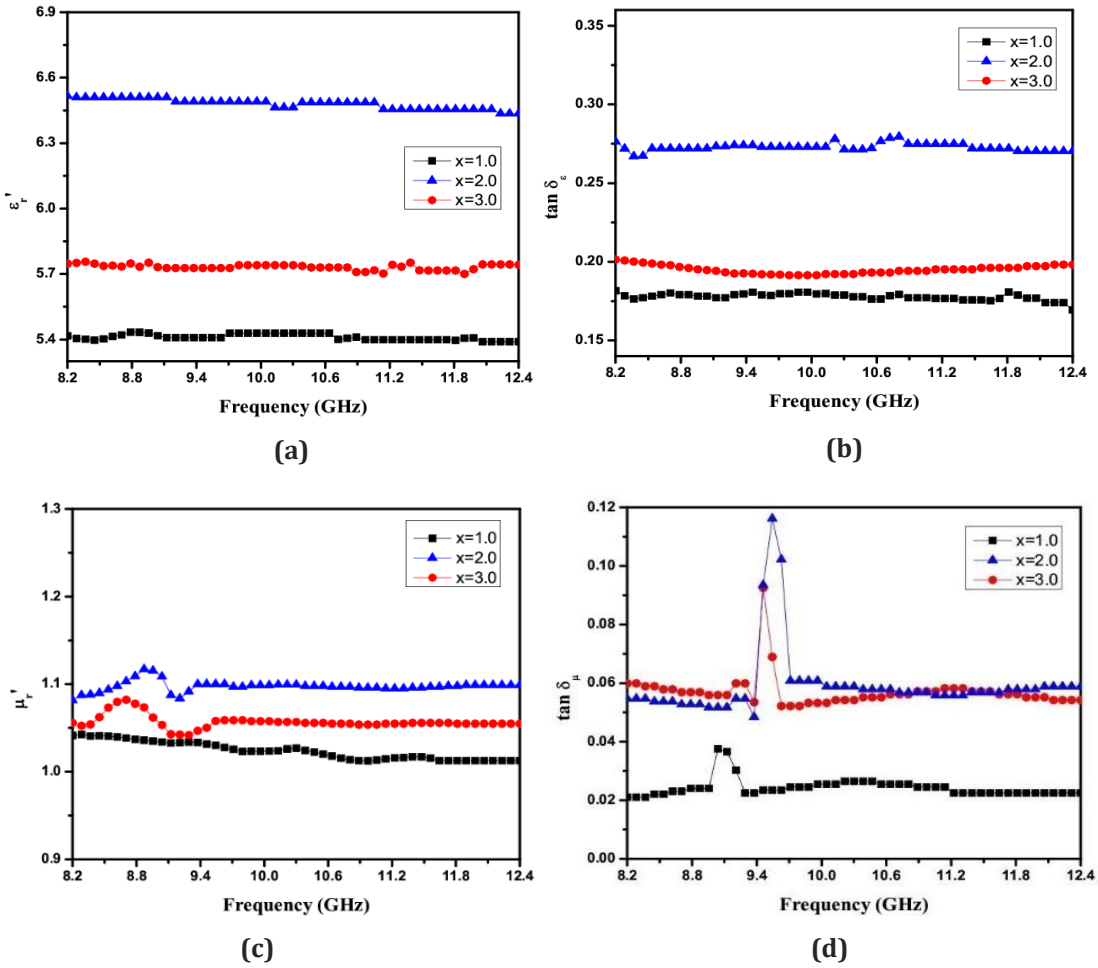

Figure 3.11: (a) ε_r', **(b)** *tan* δ_ε, **(c)** μ_r' and **(d)** *tan* δ_μ of $SrAl_xFe_{12-x}O_{19}$ (x = 1.0 to 3.0)

The ferromagnetic resonance frequency (f_r) follows the relation

$$f_r = \frac{\gamma}{2\pi} H_a \tag{3.1}$$

where γ is the gyromagnetic ratio and H_a is the anisotropy field. Thus, the natural resonance frequency (f_r), corresponding to peak in μ_r' and μ_r'', shifts towards the higher side. The value of μ_r' and μ_r'' increases when $x \geq 2.0$ in the $SrAl_xFe_{12-x}O_{19}$-LLDPE nano-composite.

The real part of the complex permittivity, ε_r' and $tan\ \delta_\varepsilon \left(= \frac{\varepsilon_r''}{\varepsilon_r'}\right)$ for $SrCo_xFe_{12-x}O_{19}$-LLDPE nanocomposites for different values of x over the X-band are plotted in figure 3.12 (a and b). Some fluctuation in the permittivity spectra is observed. When *em* wave impinges on the magneto-dielectric molecule, the electrons of the molecule interact with the *em* wave at different frequencies leading to fluctuations of the polarization of the molecule [3, 21].

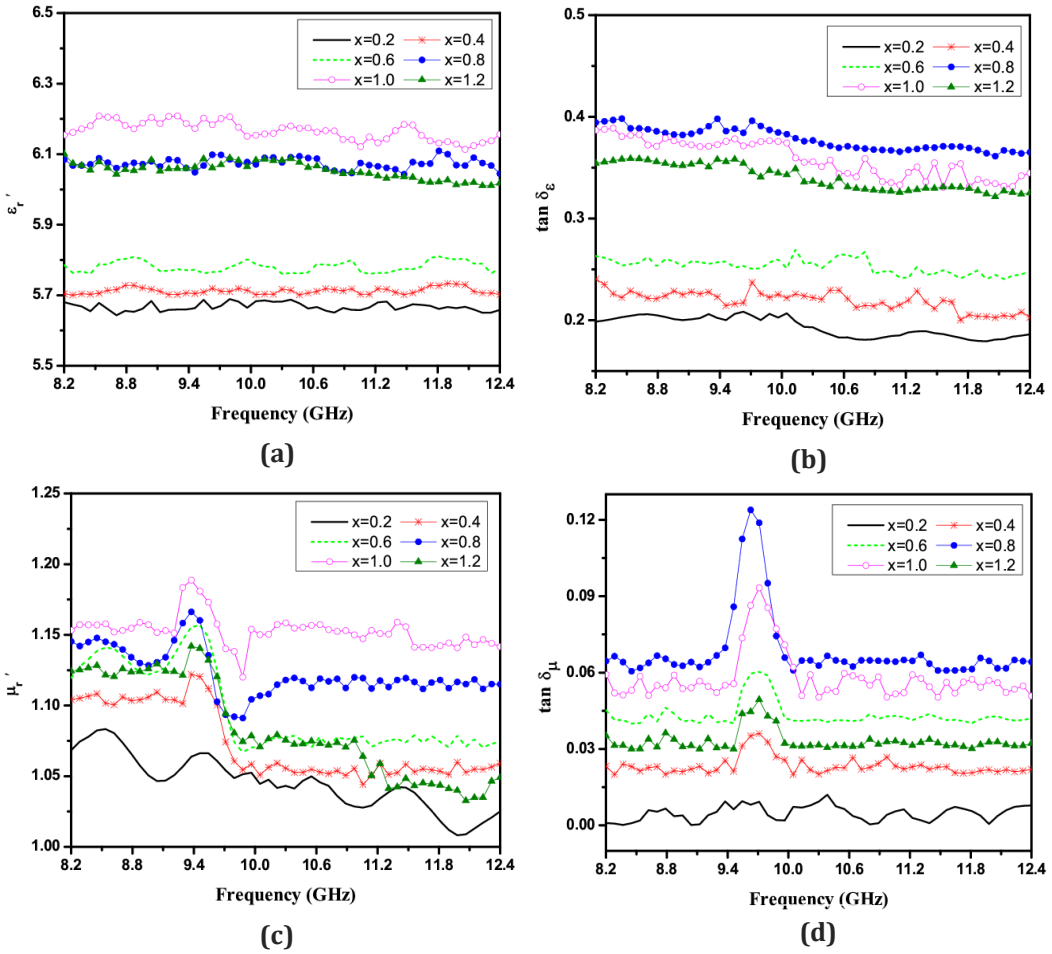

Figure 3.12: (a) ε_r', **(b)** *tan* δ_ε, **(c)** μ_r' and **(d)** *tan* δ_μ of $SrCo_xFe_{12-x}O_{19}$ (x = 0.2 to 1.2)

For $SrCo_xFe_{12-x}O_{19}$-LLDPE, increase in ε_r' is observed with inclusion of cobalt ions. In M-type ferrites, it is reported that cobalt ions tend to occupy octahedral site, replacing iron ions [18, 22]. This subdues the exchange phenomenon between ferric and ferrous ions at the octahedral site leading to increase in the complex permittivity values. With further increase of cobalt dopant, the iron ions from octahedral sites migrate to tetrahedral sites, enhancing the electron hopping and thereby lowering the complex permittivity [23, 24]. Increasing *x* values beyond 0.8 shows a decreasing trend for $tan\ \delta_\varepsilon$. The space charge carriers in a dielectric require a finite time to line up their axes parallel to the alternating microwave electric field. Cobalt ions, due to its degeneracy [15], exhibit a phenomenon of spin-orbit stabilization as a result of coupling between lattice-orbital interaction and spin dipoles by ferromagnetic exchange interactions. The spin-orbit coupling contributes to spin lattice relaxations. With increase in cobalt content beyond a certain limit, the relaxation frequency becomes comparable with the driving frequency, resulting in reduction in $tan\ \delta_\varepsilon$ values. Real part of complex permeability, μ_r' and $tan\ \delta_\mu \left(=\frac{\mu_r''}{\mu_r'}\right)$ are plotted in figure 3.12 (c & d). The resonant behavior in the complex permeability observed is due to natural resonance phenomenon which causes the permeability to increase before dropping, resulting in a resonance frequency around gyromagnetic critical frequency, also known as the spin relaxation frequency which is very close to the resonance frequency in the GHz range [25]. According to the ferromagnetic resonance theory, the resonance frequency (f_r) is proportional to the anisotropy field (H_a), which is expressed by equation (3.1). M-type hexagonal ferrites have large crystalline magnetic anisotropy and shows f_r in the range of 50-60 GHz. The magneto-crystalline anisotropy energy density is given by $E=\left(K_1-K_2\right)\sin^2\theta$ where the effective anisotropy constant ($K=K_1-K_2$) is an average contribution of anisotropy energy due to the iron ions (K_1) and the cobalt ions (K_2). Cobalt ions contribute to the magnetic anisotropy change in substituted hexaferrites [26]. Cobalt substitutes iron at the octahedral sites, leading to reduction in overall magnetic anisotropy. Cobalt substituted strontium ferrite is reported to become positive beyond a certain limit, thus, lowering the effective anisotropy [27]. Thus, substitution of iron ions with cobalt ions in octahedral sites results in decrease of anisotropy, thus, shifting f_r to the lower side. It is reported by Dionne [16] and Wartewig [28] that large relaxation time usually

gives lower anisotropy values resulting in higher permeability values. Cobalt is reported to be good relaxers due to its degenerate states, hence increase in cobalt content results in increase in μ_r. Beyond a certain content of cobalt (for $x > 0.8$), the anisotropy of cobalt substituted strontium ferrite becomes positive causing the complex permeability to drop.

3.3 Design of a single layer absorber using transmission line model

Single layer absorber is designed in the X-band for all the compositions of $SrAl_xFe_{12-x}O_{19}$-LLDPE and $SrCo_xFe_{12-x}O_{19}$-LLDPE nano-composites and the complex input impedance, Z_{in}, is determined for thickness, t=1 mm to 4 mm in steps of 0.5 mm. Table 3.3 and 3.4 gives the real (Z_{in}') and imaginary (Z_{in}'') values of input impedance for different thicknesses and different values of x.

The real and imaginary part of impedance with t = 3 mm, for all the compositions, show better matching of impedance with free space.

Table 3.3: Real & Imaginary part of Input impedance, resonance frequency with different t for $SrAl_xFe_{12-x}O_{19}$-LLDPE nano-composite with varying aluminium (x=1.0 to 3.0)

$SrAl_xFe_{12-x}O_{19}$-LLDPE									
	x=1.0			x=2.0			x=3.0		
t (mm)	**f_r (GHz)**	**Z_{in}' (Ω)**	**Z_{in}'' (Ω)**	**f_r (GHz)**	**Z_{in}' (Ω)**	**Z_{in}'' (Ω)**	**f_r (GHz)**	**Z_{in}' (Ω)**	**Z_{in}'' (Ω)**
1.0	11.89	13.28	118.70	9.54	10.04	144.33	9.21	5.43	100.55
1.5	11.89	28.12	180.07	9.54	59.00	295.20	9.21	30.95	255.96
2.0	11.89	102.39	310.88	9.54	243.93	348.30	9.21	115.97	399.45
2.5	11.89	508.05	432.35	9.54	475.48	71.41	12.31	810.50	315.65
3.0	9.88	392.11	-209.00	9.54	389.32	-0.91	9.29	279.98	-121.08
3.5	8.70	207.41	-217.71	9.71	400.34	-73.63	9.20	618.18	-201.66
4.0	8.20	560.46	-365.04	9.71	395.64	-110.06	9.29	519.98	-129.43

Table 3.4: Real & Imaginary part of Input impedance, resonance frequency with different thicknesses for $SrCo_xFe_{12-x}O_{19}$-LLDPE nano-composite with varying cobalt (x=0.2 to 1.2)

	$SrCo_xFe_{12-x}O_{19}$-LLDPE																	
	***x*=0.2**			***x*=0.4**			***x*=0.6**			***x*=0.8**			***x*=1.0**			***x*=1.2**		
t (mm)	**f_r (GHz)**	**Z_{in}' (Ω)**	**Z_{in}'' (Ω)**	**f_r (GHz)**	**Z_{in}' (Ω)**	**Z_{in}'' (Ω)**	**f_r (GHz)**	**Z_{in}' (Ω)**	**Z_{in}'' (Ω)**	**f_r (GHz)**	**Z_{in}' (Ω)**	**Z_{in}'' (Ω)**	**f_r (GHz)**	**Z_{in}' (Ω)**	**Z_{in}'' (Ω)**	**f_r (GHz)**	**Z_{in}' (Ω)**	**Z_{in}'' (Ω)**
1.0	9.70	4.84	91.02	9.62	3.20	89.65	9.71	2.65	87.90	11.47	3.60	100.88	11.14	4.71	86.12	11.47	5.23	88.29
1.5	12.40	16.02	213.03	9.62	11.73	149.22	9.71	9.59	148.39	12.40	19.92	200.33	11.47	15.24	166.26	11.47	17.44	156.35
2.0	12.40	77.84	414.19	9.62	42.51	233.33	12.40	118.60	420.99	12.40	106.76	399.60	9.71	65.37	309.53	9.71	95.80	419.78
2.5	12.40	107.70	358.47	12.06	600.36	582.92	12.40	1042.80	310.89	12.40	1106.60	467.44	9.71	200.12	495.17	9.71	301.46	695.02
3.0	10.88	387.21	-242.54	9.62	460.10	-205.11	9.71	217.35	-266.21	9.71	557.90	13.37	9.71	594.30	-235.10	9.71	619.76	-292.31
3.5	10.30	683.91	-367.69	9.62	900.10	294.05	9.71	565.34	476.94	9.71	559.00	-289.43	9.37	615.30	-301.52	9.30	660.90	-298.07
4.0	8.62	303.63	-397.66	9.71	164.39	-243.75	9.71	699.78	-332.23	8.20	673.36	-212.22	8.20	715.06	-241.22	8.24	655.71	-200.54

3.4 Absorption studies

Theoretical computation of reflection loss of $SrAl_xFe_{12-x}O_{19}$-LLDPE and $SrCo_xFe_{12-x}O_{19}$-LLDPE nanocomposites are carried out in each composition. Based on the theoretical results, a single layer metal backed absorber is fabricated and tested for microwave absorption over the X-band.

3.4.1 Computed microwave absorption using TLM

The thickness of the absorber sample is varied from 1 mm to 4 mm in steps of 0.5 mm for all the $SrAl_xFe_{12-x}O_{19}$-LLDPE and $SrCo_xFe_{12-x}O_{19}$-LLDPE nano-composites. Reflection loss for $SrAl_xFe_{12-x}O_{19}$-LLDPE composites is calculated with *t* varying from 1 mm to 4 mm and are given in figure 3.13.

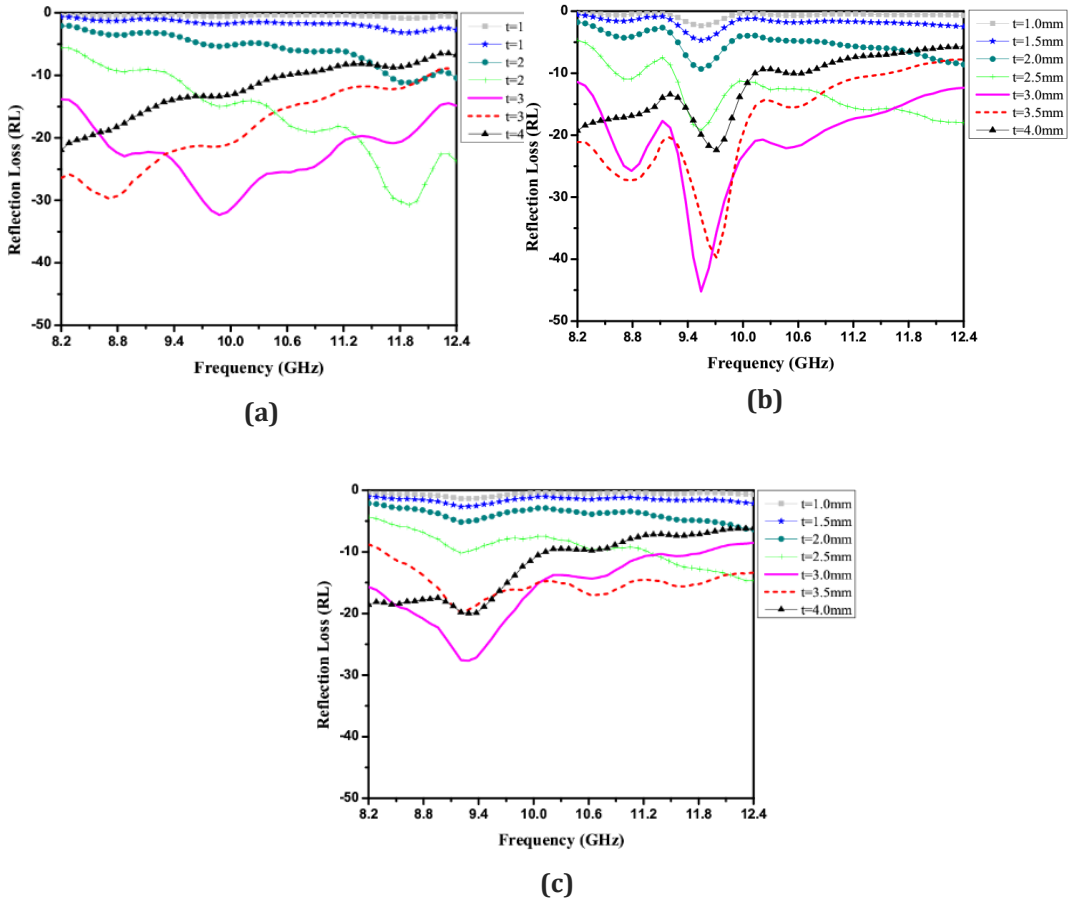

Figure 3.13: *RLc* of of $SrAl_xFe_{12-x}O_{19}$-LLDPE composite **(a)** x=1.0, **(b)** x=2.0, **(c)** x=3.0 (Calculated)

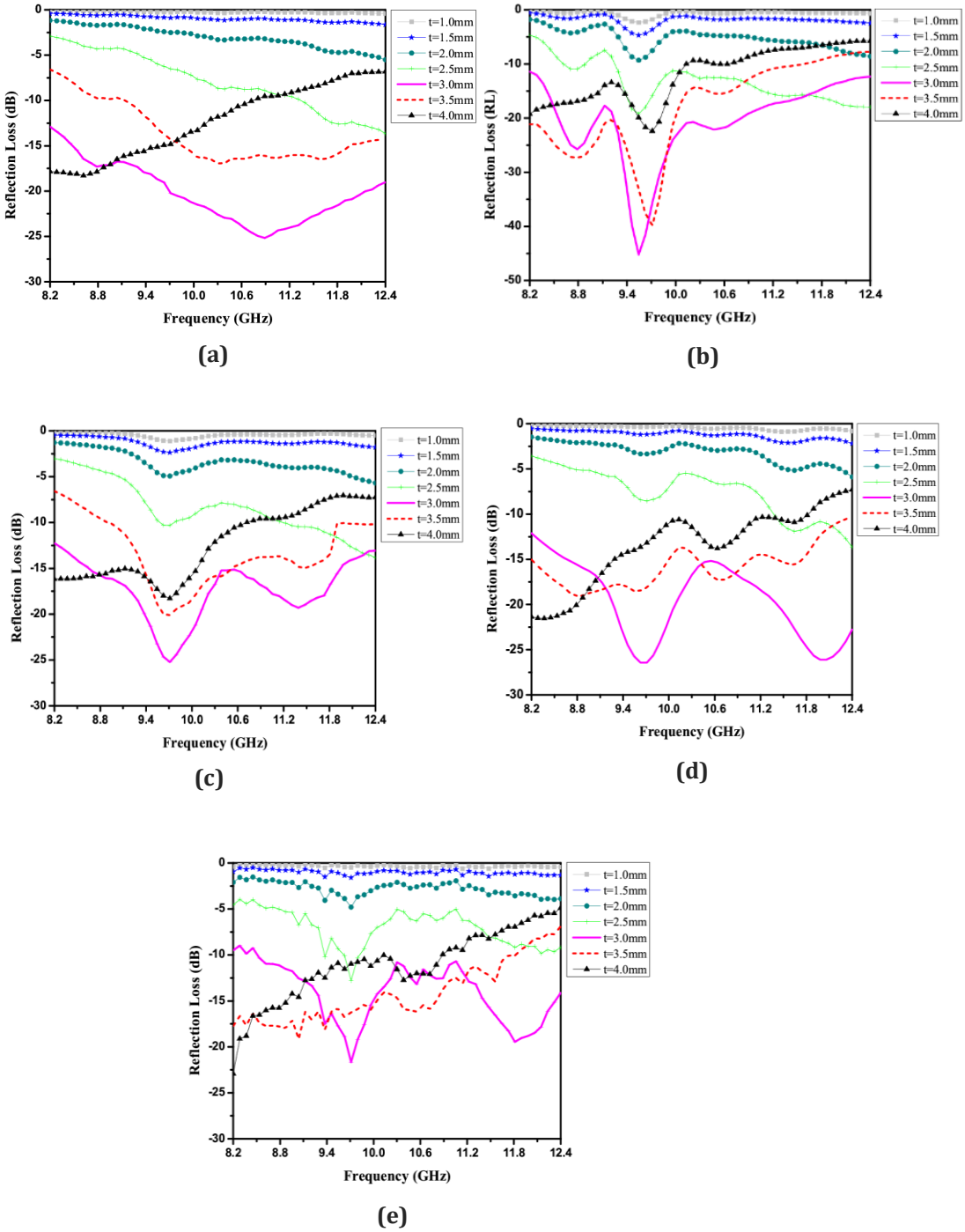

Figure 3.14: *RL*$_c$ of $SrCo_xFe_{12-x}O_{19}$-LLDPE composite **(a)** x=0.2, **(b)** x=0.4, **(c)** x=0.6, **(d)** x=0.8, **(e)** x=1.0 (Calculated)

Reflection loss for $SrCo_xFe_{12-x}O_{19}$-LLDPE composites with *t* varying from 1 mm to 4 mm and are given in figure 3.14. The detail of calculated reflection loss (*RL*$_c$) along with for all the compositions are summarized in table 3.5 and table 3.6.

Table 3.5: Calculated reflection loss (RL_c), resonant frequency (f_r) and calculated -10 dB absorption bandwidth (BW_c) with varying t of $SrAl_xFe_{12-x}O_{19}$-LLDPE nanocomposites

	$SrAl_xFe_{12-x}O_{19}$-LLDPE								
	x=1.0			x=2.0			x=3.0		
t (mm)	**RL_c (dB)**	**f_r (GHz)**	**BW_c (GHz)**	**RL_c (dB)**	**f_r (GHz)**	**BW_c (GHz)**	**RL_c (dB)**	**f_r (GHz)**	**BW_c (GHz)**
1.0	-0.84	11.89	-	-2.34	9.54	-	-1.36	9.21	-
1.5	-3.15	11.89	-	-4.69	9.54	-	-2.67	9.21	-
2.0	-11.14	11.89	0.30	-9.31	9.54	-	-5.16	9.21	-
2.5	-30.70	11.89	3.03	-19.21	9.54	3.11	-14.67	12.31	1.10
3.0	-32.33	9.88	4.20	-45.23	9.54	4.20	-27.64	9.29	3.61
3.5	-29.71	8.70	3.86	-39.77	9.71	3.36	-19.88	9.20	4.04
4.0	-21.93	8.20	2.35	-22.41	9.71	2.43	-19.97	9.29	1.93

The results show that for a thickness of t = 3 mm, maximum reflection loss is obtained. As, the thickness satisfies the condition of destructive interference at a particular frequency, the reflection loss is found to be maximum at that frequency. Sheets of thickness 3 mm are fabricated for experimental evaluation of absorption performance for all the compositions.

Table 3.6: Calculated reflection loss (RL_c), resonant frequency (f_r) and calculated -10 dB absorption bandwidth (BW_c) with varying t of $SrCo_xFe_{12-x}O_{19}$-LLDPE nanocomposites

	$SrCo_xFe_{12-x}O_{19}$-LLDPE																	
	x=0.2			x=0.4			x=0.6			x=0.8			x=1.0			x=1.2		
t (mm)	**RL_c (dB)**	**f_r (GHz)**	**BW_c (GHz)**	**RL_c (dB)**	**f_r (GHz)**	**BW_c (GHz)**	**RL_c (dB)**	**f_r (GHz)**	**BW_c (GHz)**	**RL_c (dB)**	**f_r (GHz)**	**BW_c (GHz)**	**RL_c (dB)**	**f_r (GHz)**	**BW_c (GHz)**	**RL_c (dB)**	**f_r (GHz)**	**BW_c (GHz)**
1.0	-0.2	9.7	-	-1.3	9.6	-	-1.1	9.7	-	-1.0	11.4	-	-0.6	11.1	-	-0.5	11.4	-
1.5	-1.6	12.4	-	2.7	9.6	-	-2.3	9.7	-	-2.2	12.4	-	-1.4	11.4	-	-1.1	11.4	-
2.0	-5.4	12.4	-	-5.4	9.6	-	-5.6	12.4	-	-6.0	12.4	-	-4.7	9.7	-	-5.7	9.7	-
2.5	-13.6	12.4	1.0	-11.8	12.0	0.8	-13.8	12.4	1.8	-14.0	12.4	1.01	-12.7	9.7	0.17	-13.8	9.7	0.10
3.0	-25.1	10.8	4.2	-25.8	9.6	4.2	-25.2	9.7	4.2	-28.2	9.7	4.20	-21.6	9.7	3.87	-20.2	9.7	3.80
3.5	-16.9	10.3	3.1	-20.5	9.6	3.1	-20.0	9.7	3.4	-19.5	9.7	4.20	-18.1	9.3	3.61	-14.0	9.3	3.03
4.0	-18.3	8.6	2.5	-18.7	9.7	2.1	-18.2	9.7	2.4	-21.7	8.2	3.50	-22.1	8.2	2.6	-20.4	8.2	1.7

3.4.2 Measured microwave absorption

The measured reflection loss (RL_m) and calculated reflection loss (RL_c) spectra for of $SrAl_xFe_{12-x}O_{19}$-LLDPE and $SrCo_xFe_{12-x}O_{19}$-LLDPE nano-composites with for t = 3 mm are given in figure 3.15 and 3.16.

A maximum RL of -26.7 dB and -10 dB absorption bandwidth of 2.86 GHz (11.64-8.78 GHz) over the X-band is found for 60 wt. % for $SrAl_xFe_{12-x}O_{19}$-LLDPE composite (x = 2). The decrease in ε_r and μ_r with increase in x beyond 2.0 leads to lower loss tangent values which in turn affects absorption. $SrCo_xFe_{12-x}O_{19}$-LLDPE nano-composite with x = 0.2 shows -16.3 dB at 11.2 GHz.

With the increase in cobalt ions in $SrCo_xFe_{12-x}O_{19}$, two distinct absorption peaks >-10 dB are observed (figure 3.16). The sample with x = 0.8, shows a -10 dB absorption bandwidth of 3.56 GHz (8.84 GHz-12.4 GHz) and two absorption peaks of -21.2 dB at 9.3 GHz and -19.1 dB at 11.7 GHz in the *RL* envelope. The decrease in ε_r and μ_r with increase in x beyond 0.8 leads to lower loss tangent values affecting the absorption.

From the Figure 3.15 and 3.16, it can be seen that the resonant frequency of RL_m and RL_c are in close proximity; the small shift in frequency could be due to fabrication tolerance. Also, practically, the absorber is designed for specific thickness satisfying the condition of destructive interference at a particular frequency. The designed thickness may not satisfy this condition over the entire X-band leading to lower measured -10 dB absorption bandwidth as compared to calculated. However, maximum RL is observed for 3 mm thick samples, for both the modelled and fabricated absorbers.

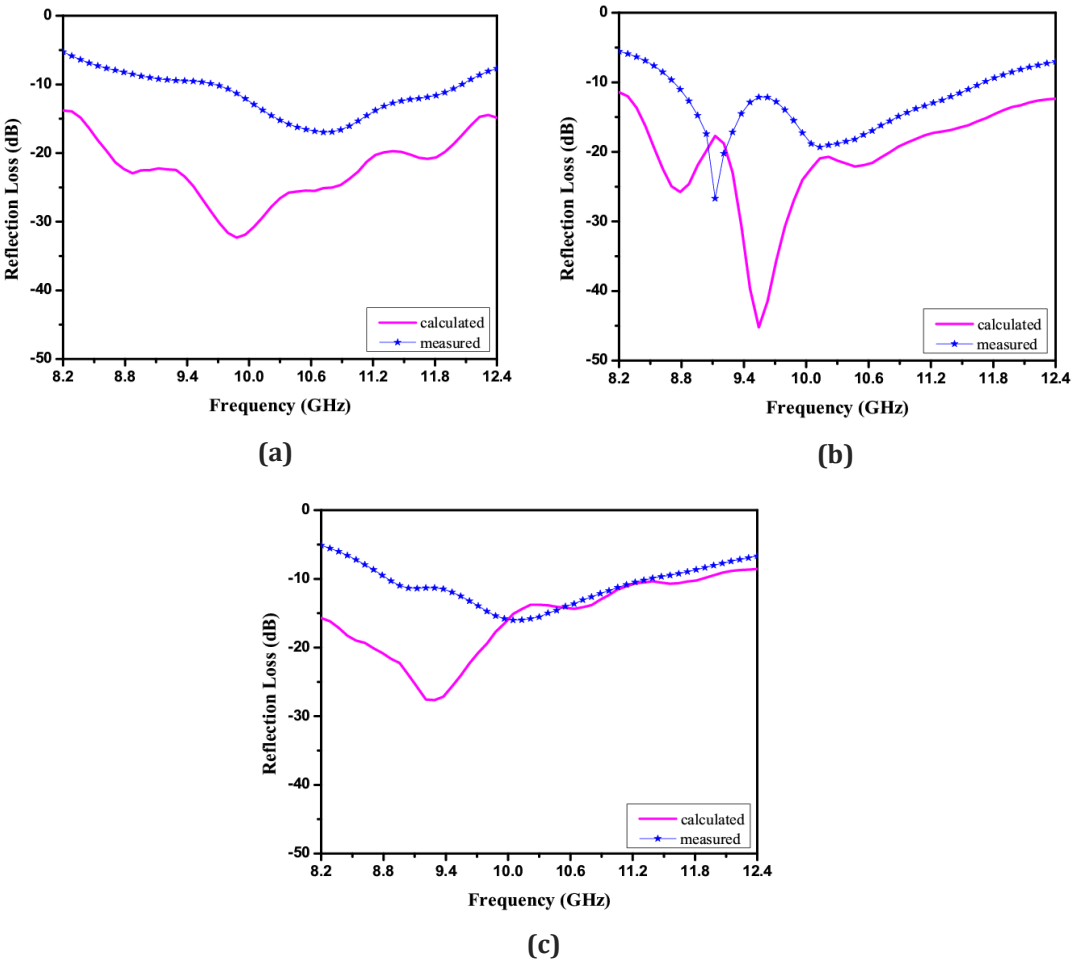

Figure 3.15: Measured and calculated *RL* $SrAl_xFe_{12-x}O_{19}$-LLDPE composite with t = 3mm **(a)** x = 1.0, **(b)** x = 2.0 and **(c)** x = 3.0

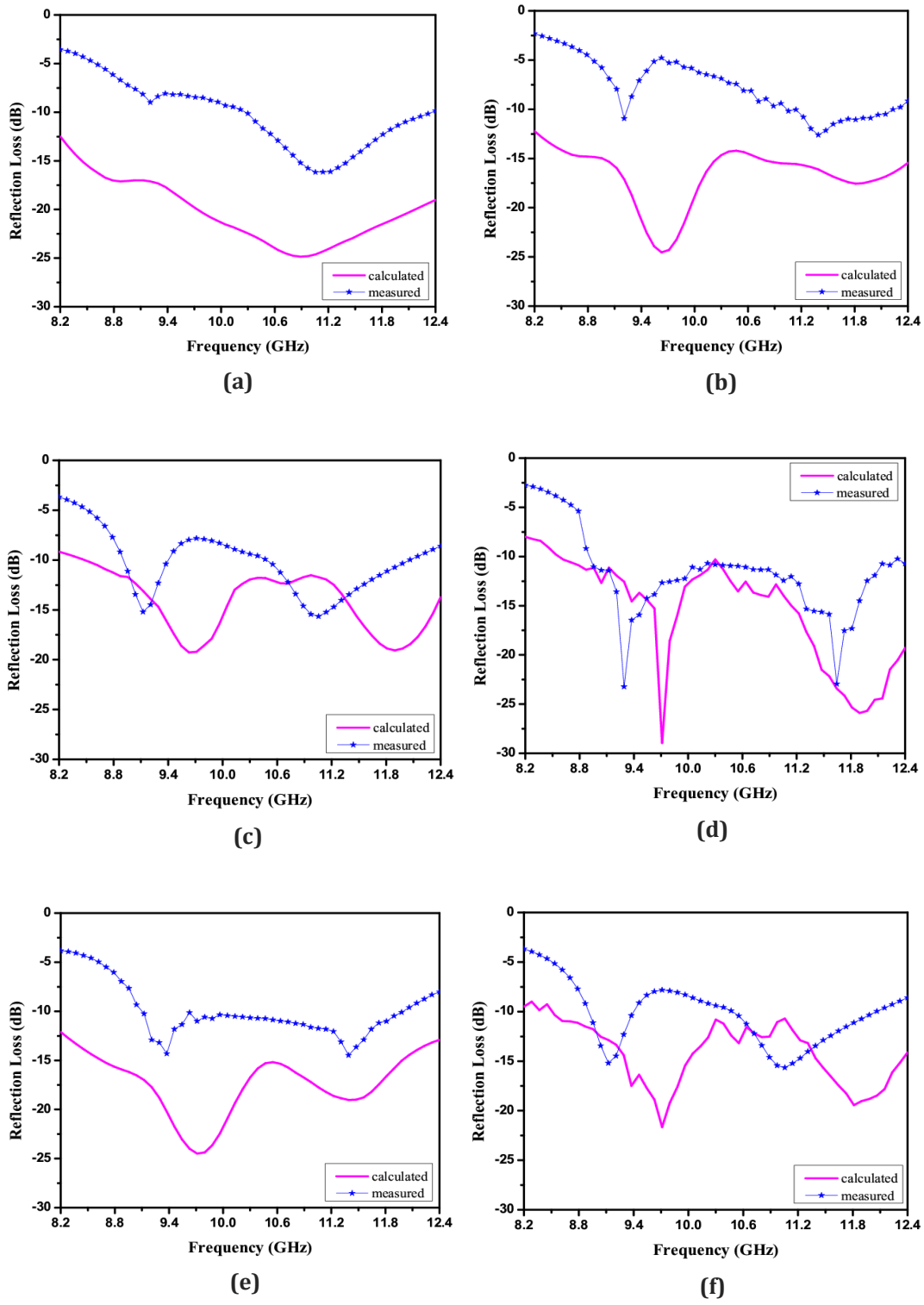

Figure 3.16: Measured and calculated *RL* of $SrCo_xFe_{12-x}O_{19}$-LLDPE composite with t = 3mm **(a)** x = 0.2, **(b)** x = 0.4, **(c)** x = 0.6, **(d)** x = 0.8, **(e)** x = 1.0 and **(f)** x = 1.2

The attenuation constant, α, of the $SrAl_xFe_{12-x}O_{19}$-LLDPE and $SrCo_xFe_{12-x}O_{19}$-LLDPE nano-composites is calculated for X-band from the measured ε_r and μ_r values of the composites. The attenuation spectra follow the resonant behavior of complex permeability of the ferrite. The attenuation constant

obtained for $SrCo_xFe_{12-x}O_{19}$-LLDPE nano-composite is maximum for x = 0.8 which is 79.89 dB/cm at 9.5 GHz. The percentage absorption is given in figure 3.17.

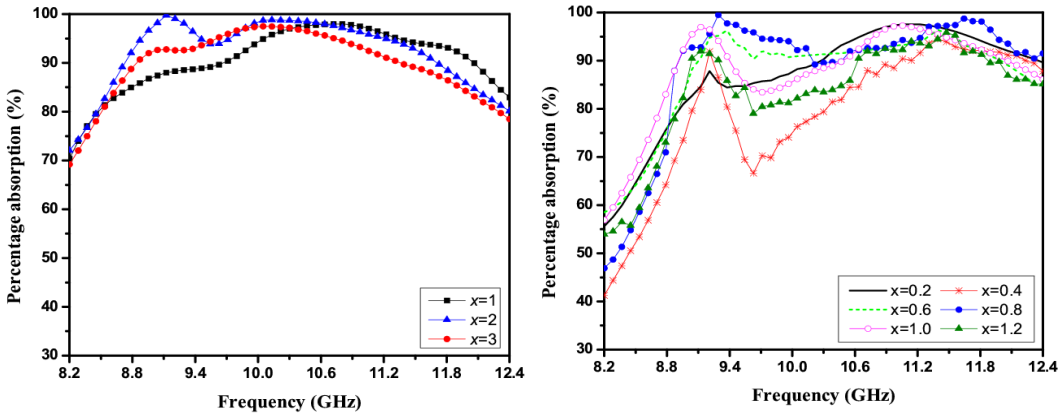

Figure 3.17: Attenuation constant

(a) $SrAl_xFe_{12-x}O_{19}$-LLDPE (x = 1.0 to 3.0)

(b) $SrCo_xFe_{12-x}O_{19}$-LLDPE (x = 0.2 to 1.2)

Table 3.7 gives a summary of the absorption performance of $SrAl_2Fe_{10}O_{19}$-LLDPE and $SrCo_{0.8}Fe_{11.2}O_{19}$-LLDPE nano-composites. Absorption performance of other reported work in the X-band using strontium ferrite as filler is presented in table 3.8 along with the present work.

Table 3.7: Absorption performance of $SrAl_2Fe_{10}O_{19}$-LLDPE and $SrCo_{0.8}Fe_{11.2}O_{19}$-LLDPE nano composites ($t$=3 mm)

Ferrite compositions	RL_m (dB)	f_r (GHz)	-10 dB absorption bandwidth	% absorption
$SrAl_2Fe_{10}O_{19}$-LLDPE	-26.7	9.12	2.86 GHz (8.78 -11.64 GHz)	99.76 %
$SrCo_{0.8}Fe_{11.2}O_{19}$-LLDPE	-23.2	9.3	3.56 GHz (8.84 GHz-12.4 GHz)	99.52 %

Table 3.8: Comparison of microwave absorbing properties of recent reported doped single layer absorbers

Material composition	Thickness (mm)	Max RL (dB)		-10 dB bandwidth (GHz)	
		Theor.	Exp.	Theor.	Exp.
$SrFe_{11.2}Zn_{0.8}O_{19}$ in epoxy resin [29]	2.5	-29.81	-	2.77	-
$Sr_{1.96}Gd_{0.04}Co_2Fe_{27.80}Mn_{0.2}O_{46}$ in paraffin wax [30]	3.5	-25.2	-	1.50	-
$SrZn_{2x}Co_xFe_{16}O_{27}$ in epoxy resin [31]	4.5	-28.0	-	2.10	-
$SrAl_2Fe_{10}O_{19}$-LLDPE	**3.0**	-45.23	**-26.7**	4.20	**2.86**
$SrCo_{0.8}Fe_{11.2}O_{19}$-LLDPE	**3.0**	-39.70	**-23.2**	4.20	**3.56**

3.5 Conclusion

In this chapter, the studies conducted show that addition of cobalt enhances the absorption properties of M-type strontium ferrite-LLDPE nano-composite in X-band. The sample $SrCo_{0.8}Fe_{11.2}O_{19}$-LLDPE nanocomposite with thickness 3 mm shows more than 90 % absorption over the X-band with two distinct absorption peaks of ~ -20 dB. In case of $SrAl_2Fe_{10}O_{19}$-LLDPE nanocomposite, it shows a bandwidth of 2.86 GHz (8.78-11.64 GHz). Studies conducted on the effect of two different doping elements on $SrFe_{12}O_{19}$ show that bandwidth of $SrCo_{0.8}Fe_{11.2}O_{19}$-LLDPE nanocomposite covers the absorption bandwidth of $SrAl_2Fe_{10}O_{19}$-LLDPE nano-composites. Therefore, for multilayer studies, $SrCo_{0.8}Fe_{11.2}O_{19}$-LLDPE nanocomposite and $SrFe_{12}O_{19}$-LLDPE nanocomposites are considered.

References:

[1] Qiao, L., You, L., Zheng, J., Jiang, L. and Sheng, J. (2007). The magnetic properties of strontium hexaferrites with La–Cu substitution prepared by SHS method. *Journal of Magnetism and Magnetic Materials*, 318: 74–78.

[2] Ounnunkada, S. and Winotai, P. (2006). Properties of Cr-substituted M-type barium ferrites prepared by nitrate–citrate gel-autocombustion process. *Journal of Magnetism and Magnetic Materials*, 301: 292–300.

[3] Ozah, S. and Bhattacharyya, N. S. (2015). Development of $BaAl_xFe_{12-x}O_{19}$-NPR nanocomposite as an efficient absorbing material in the X-band. *Journal of Magnetism and Magnetic Materials*, 374: 516–524.

[4] Liu, M., Shen, X., Song, F., Xiang, J. and Meng, X. (2011). Microstructure and magnetic properties of electrospun one-dimensional Al^{3+}-substituted $SrFe_{12}O_{19}$ nanofibers. *Journal of Solid State Chemistry*, 184: 871–876.

[5] Ebrahimi, S. A. S., Khanmohammadi, H. and Masoudpanah, S. M. (2015). Effects of High-Energy Ball Milling on the Microwave Absorption Properties of $Sr_{0.9}Nd_{0.1}Fe_{12}O_{19}$. *Journal of Superconductivity and Novel Magnetism*, 28 2715–2720.

[6] Choopani, S., Keyhan, N., Ghasemi, A., Sharbati, A. and Alam, R. S. (2009). Structural, magnetic and microwave absorption characteristics of $BaCo_xMn_xTi_{2x}Fe_{12-4x}O_{19}$. *Materials Chemistry and Physics*, 113: 717–720.

[7] Alam, R. S., Moradi, M., Nikmanesh, H., Ventura, J. and Rostami, M. (2016). Magnetic and microwave absorption properties of $BaMg_{x/2}Mn_{x/2}Co_xTi_{2x}Fe_{12-4x}O_{19}$ hexaferrite nanoparticles. *Journal of Magnetism and Magnetic Materials*, 402: 20–27.

[8] Zhou, Z., Wang, Z., Wang, X., Li, Q., Jin, M. and Xu, J. (2015). Preparation and magnetic properties of Nd–Co-substituted M-type strontium ferrite by microwave-assisted synthesis method. *Journal of Superconductivity and Novel Magnetism*, 28: 1773–1778.

[9] Baniasadi, A., Ghasemi, A., Nemati, A., Ghadikolaei, M. A. and Paimozd, E. (2014). Effect of Ti–Zn substitution on structural, magnetic and microwave absorption characteristics of strontium hexaferrite. *Journal of Alloys and Compounds*, 583: 325–328.

[10] Chawla, S. K., Meena, S. S., Kaur, P., Mudsainiyan, R. K. and Yusuf, S. M. (2015). Effect of site preferences on structural and magnetic switching properties of Co–Zr doped strontium hexaferrite $SrCo_xZr_xFe_{(12-2x)}O_{19}$. *Journal of Magnetism and Magnetic Materials*, 378: 84–91.

[11] Kools, F., Morela, A., Grossinger, R., Le Bretond, J.M. and Tenaud, P. (2002). LaCo-substituted ferrite magnets, a new class of high-grade ceramic magnets; intrinsic and microstructural aspects. *Journal of Magnetism and Magnetic Materials*, 242: 1270–1276.

[12] Zhang, Z., Liu, X., Wang, X., Wu, Y. and Li, R. (2012). Effect of Nd–Co substitution on magnetic and microwave absorption properties of $SrFe_{12}O_{19}$ hexaferrites. *Journal of Alloys and Compounds*, 525: 114–119.

[13] Luo, H., Rai, B. K., Mishra, S. R., Nguyen, V. V. and Liu, J. P. (2012). Physical and magnetic properties of highly aluminum doped strontium ferrite nanoparticles prepared by auto-combustion route. *Journal of Magnetism and Magnetic Materials*, 324: 2602–2608.

[14] Wang, S., Ding, J., Shi, Y. and Chen, Y. J. (2000). High coercivity in mechanically alloyed $BaFe_{10}Al_2O_{19}$. *Journal of Magnetism and Magnetic Materials*, 219 (2): 206–212.

[15] Goodenough, J. B. *Magnetism and Chemical Bond.* Wiley, New York, 214, 1963.

[16] Dionne, G. F. (1988). Theory of Co^{2+} exchange isolation in ferrimagnetic spinels and garnets. *Journal of applied physics*, 64: 1323–1331.

[17] Qiu, J., Zhang, Q., Gu, M. and Shen H. (2005). Effect of aluminium substitution on microwave absorption properties of barium hexaferrite. *Journal of applied physics*, 98: 103905-1-5.

[18] Xie, T., Xu, L. and Liu, C. (2012). Synthesis and properties of composite magnetic material $SrCo_xFe_{12-x}O_{19}$ (x=0–0.3). *Powder Technology*, 232: 87-92.

[19] Luo, H., Rai, B. K., Mishra, S. R., Nguyen, V.V. and Liu, J. P. (2012). Physical and magnetic properties of highly aluminum doped strontium ferrite nanoparticles prepared by auto-combustion route. *Journal of Magnetism and Magnetic Materials*, 324: 2602–2608.

[20] El-Sayed, S. M., Meaz, T. M., Amer, M. A. and ElShersa H. A. (2013). Magnetic behavior and dielectric properties of aluminum substituted M-type barium hexaferrite. *Physica B*, 426: 137–143.

[21] Griffiths, D. J. *Introduction to Electrodynamics*. 3rd edition, PHI Learning Private Limited, New Delhi, 2011.

[22] Kishimoto, M., Kitahata, S. and Amemiya, M. (2011). Structural and magnetic properties of $BaCo_xFe_{12-x}O_{19}$ (x=0.2, 0.4, 0.6, 1) nanoferrites synthesized via citrate sol-gel method. *Journal of applied physics*, 61: 101–104.

[23] Iqbal, M. J., Ashiq, M. N. and Gomez, P. H. (2009). Effect of doping of Zr-Zn binary mixtures on structural, electrical and magnetic properties of Sr-hexaferrite nanoparticles. *Journal of Alloys and Compounds*, 478: 736–740.

[24] Ghahfarokhi, S. E. M., Ranjbar, F. and Shoushtari, M. Z. (2014). A study of the properties of $SrFe_{12-x}Co_xO_{19}$ nanoparticles. *Journal of Magnetism and Magnetic Materials*, 349: 80–87.

[25] Pullar, R. C. (2012). Hexagonal ferrites: A review of the synthesis, properties and applications of hexaferrite ceramics. *Progress in Material Science*, 57: 1191–334.

[26] Batlle, X., Obradors, X., Pernet, M., Vallet, M., Cabanas, M., Rodriguez, J. and Fontcuberta, J. (1990). Cationic distribution, magnetization and magnetic anisotropy of Co^{2+} doped M-type barium ferrite. *Journal of Magnetism and Magnetic Materials*, 83: 465–467.

[27] De Bitetto, D. J. (1964). Anisotropy Fields in Hexagonal Ferrimagnetic Oxides by Ferrimagnetic Resonance. *Journal of applied physics*, 35: 3482-3487.

[28] Wartewig, P., Krause, M. K., Esquinazi, P., Rosler, S. and Sonntag, R. (1999). Magnetic properties of Zn- and Ti-substituted barium hexaferrite. *Journal of Magnetism and Magnetic Materials*, 192: 83–99.

[29] Tyagi, S., Baskey, H. B., Agarwala, R. C., Agarwala, V. and Shami, T. C. (2011). Synthesis and characterization of $SrFe_{11.2}Zn_{0.8}O_{19}$ nanoparticles for enhanced microwave absorption. *Journal of Electronic Materials*, 40 (9):2004–2014.

[30] Sadiq, I., Naseem, S., Ashiq, M. N., Khan, M. A., Niaz, S. and Rana, M. U. (2016). Tunable microwave absorbing nano-material for X-band applications. *Journal of Magnetism and Magnetic Materials*, 401: 63–69.

[31] Farhadizadeha, A.R., Ebrahimia, S.A.S. and Masoudpanahb, S.M. (2015). Magnetic and microwave absorption properties of ZnCo-substituted W-type strontium hexaferrite. *Journal of Magnetism and Magnetic Materials*, 382: 233–236.